

Comparative Analysis of Weld Microstructure in Ti-6Al-4V Samples Produced by Rolling and Wire-Feed Electron Beam Additive Manufacturing

A. V. Panin^{1,2*}, M. S. Kazachenok¹, K. V. Krukovsky¹,
L. A. Kazantseva¹, and S. A. Martynov¹

¹ *Institute of Strength Physics and Materials Science, Siberian Branch, Russian Academy of Sciences, Tomsk, 634055 Russia*

² *National Research Tomsk Polytechnic University, Tomsk, 634050 Russia*

* *e-mail: pav@ispms.ru*

Received September 30, 2022; revised February 2, 2023; accepted February 3, 2023

Abstract—The microstructure and phase composition of electron beam welded Ti-6Al-4V titanium alloy were studied by optical and scanning electron microscopy, backscattered electron diffraction, and X-ray diffraction analysis. Deep-penetration electron beam welds were made in a single pass on rectangular Ti-6Al-4V samples obtained by rolling and wire-feed electron beam additive manufacturing. It was found that the weld width in the 3D printed Ti-6Al-4V samples is greater than in the rolled material. The influence of the vapor capillary on the size, shape and structure of primary β grains formed in the fusion zone was shown. The variation of the penetration coefficient, volume fraction of the residual β phase, and residual stresses along the weld length was studied for Ti-6Al-4V samples obtained by both rolling and 3D printing.

Keywords: Ti-6Al-4V titanium alloy, electron beam welding, deep-penetration keyhole welding, additive manufacturing technology, microstructure, microhardness

DOI: 10.1134/S1029959923060048

1. INTRODUCTION

The major advantages of additive technologies are a short production cycle and the ability to form complex structural elements while reducing production costs [1, 2]. The latter is primarily due to a significant reduction in material consumption and production waste. At the same time, there are certain difficulties in the manufacture of large parts and products, which are associated with the limited dimensions of the build platform and volume of the printer chamber [3, 4]. For example, enlarging the printer chamber for powder bed fusion, which consists in applying a thin powder layer onto the platform and its subsequent selective melting with an electron or laser beam, increases considerably the amount of consumables [5]. For this reason, the method of direct energy deposition, when the gas-powder jet of metal particles or wire is fed into the electron or laser beam, is more suitable for the manufacture of large products. This method provides a higher 3D printing speed and is characterized by high efficiency of consumables.

However, it is inapplicable to the manufacture of products with complex geometry and internal structure [6, 7]. Thus, additive manufacturing of large and complex products cannot do without permanent joints. This explains the urgency of the study of the microstructure and mechanical properties of welds of additively manufactured structural elements.

Currently, permanent joints of 3D printed samples of titanium alloy Ti-6Al-4V, which accounts for more than 50% of the world production of all titanium alloys, are most commonly produced by laser welding [4, 8]. It is shown that Ti-6Al-4V samples have a similar microstructure in the weld and base metal (due to the close cooling rates of the melt pool during welding and 3D printing), predominantly consisting of columnar primary β grains with the acicular α' phase [3, 4, 8]. The size of primary β grains as well as the presence of residual porosity in 3D printed samples has a significant influence on the basic geometric parameters of the weld, such as width, thickness, convexity, and penetration depth. Thus,

the comparison of the Ti-6Al-4V samples produced by rolling and direct laser deposition showed that the 3D printed samples had larger grains and consequently a wider weld [9]. In contrast, highly porous Ti-6Al-4V samples produced by selective laser melting were characterized by a smaller weld width and depth compared to the rolled samples [10]. As a consequence, welding of the 3D printed porous products requires a greater amount of input thermal energy per unit weld length than welding of their cast analogues [10].

Laser welds usually have higher hardness compared to the base metal of the 3D printed Ti-6Al-4V sample. Welding has no influence on the tensile strength of Ti-6Al-4V alloy samples [3], but it significantly reduces their ductility and fatigue strength [4].

Despite the high cost of equipment and the need for a vacuum chamber, which limits the size of parts being welded, electron beam welding is the method of choice for permanent joining titanium alloys. This welding method provides the maximum power density (up to 10^8 W/cm²) and consequently the maximum penetration depth (from 6 to 75 mm) with the minimum width of the weld and heat-affected zone as compared to other welding methods (laser, electric arc and argon arc welding, friction stir welding, etc.) [11, 12]. Though electron beam welding of forged and cast titanium alloys finds wide industrial applications [13, 14], it is extremely poorly studied for 3D printed products. However, it was found that, during electron beam welding of Ti-6.5Al-3.5Mo-1.5Zr-0.3Si samples produced by selective laser melting, columnar primary β grains grew in the fusion zone along a temperature gradient [15]. An acicular martensitic α' phase was observed inside the grains, and the size of the martensite needles in the weld decreased as its depth increased. Due to the higher hardness of the weld metal, these samples fracture in the base metal under uniaxial tension.

The microstructure and microhardness of permanent joints of Ti-6Al-4V samples produced by wire-feed electron beam additive manufacturing were studied earlier [16]. It was shown that the process of electron beam welding was accompanied by epitaxial growth of columnar primary β grains in the fusion zone of a double-welded joint, the transverse size of which was close to the size of primary β grains in the base metal. Inside the primary β grains, α' -phase plates were formed, the size of which was 1.5 times smaller than the size of the α -phase plates in the base metal. In addition, the nanocrystalline α'' phase is

found in the fusion zone, which also contributed to an increase in the microhardness of the weld.

Greatest practical interest is in the study of the microstructure and mechanical properties of permanent joints obtained by deep-penetration electron beam welding, resulting in a narrow and deep weld. However, for 3D printed Ti-6Al-4V titanium alloy, such studies are unavailable in the literature. The aim of this work is to compare the microstructure and microhardness of deep-penetration electron beam welds of Ti-6Al-4V samples produced by rolling and wire-feed electron beam additive manufacturing.

2. INVESTIGATION PROCEDURE

The investigation was performed on as-rolled Ti-6Al-4V titanium alloy sheets with a thickness of 10 mm (GOST 22178-76) and on parallelepiped Ti-6Al-4V prints with dimensions of $25 \times 25 \times 70$ mm³ built using the wire-feed electron beam additive manufacturing unit (ISPMS SB RAS, Russia). The 3D printing process was carried out by melting the 1.6 mm Ti-6Al-4V wire in a vacuum with a pressure of 1.3×10^{-3} Pa using an electron gun with the plasma cathode at an accelerating voltage of 30 kV. The beam current was varied in the range of 17–24 mA. The distance between the electron gun and the titanium build platform plate was 630 mm. The wire was fed with the speed 2 m/min at an angle of 35° to the substrate surface. The tool path strategy for 3D printing corresponded to the pattern with mirror layer deposition. The distance between adjacent tracks within a layer was ~2 mm. After a layer is deposited, the build platform was lowered by 1.5 mm. The chemical composition of rolled Ti-6Al-4V sheets, Ti-6Al-4V wire, and Ti-6Al-4V prints determined by energy dispersive analysis is presented in Table 1.

Rectangular bars $10 \times 10 \times 55$ mm³ were cut from the rolled sheets and prints by electrical discharge cutting. Electron beam welding was simulated as a single pass of the electron beam across a rectangular bar in its central part (Fig. 1a). The focal plane of the

Table 1. Chemical composition of Ti-6Al-4V samples

Elements	Rolled samples	Wire	3D printed samples
Ti, wt %	89.6	88.6	90.7
Al, wt %	5.3	6.6	4.7
V, wt %	4.2	4.1	4.1
Impurities, wt %	0.9	0.7	0.5

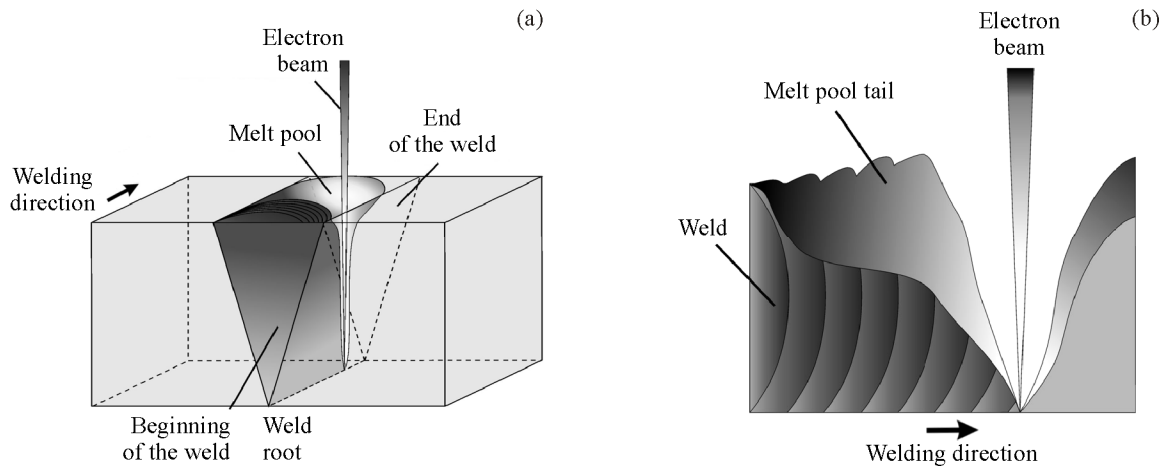


Fig. 1. Schematic of electron beam welding of Ti-6Al-4V samples (a) and melt pool dynamics (b).

electron beam was on the lower surface of the bars. In other words, the defocus distance, i.e. the distance from the surface to be welded to the focal point of the electron beam, was 10 mm. During the welding process, the bars were placed on the 10-mm-thick platform made of stainless steel 12Cr18Ni10Ti. The electron beam parameters were selected to form a complete-penetration weld (Table 2).

The geometric parameters and microstructure of welds of the rolled and 3D printed Ti-6Al-4V samples were studied using a Zeiss Axiovert 40 MAT optical microscope and an Apreo S scanning electron microscope equipped with the INCAx-act energy dispersive X-ray microanalyzer and Nordlys electron backscatter diffraction (EBSD) camera by Oxford Instruments. EBSD maps were plotted at the scanning step 0.2 μm; a grain was taken to be an area consisting of at least 5 points. To carry out metallographic studies, the test samples were previously subjected to mechanical grinding, polishing and subsequent Kroll etching.

X-ray diffraction analysis of base metal and weld metal of the rolled and 3D printed Ti-6Al-4V samples was carried out on a Shimadzu XRD-7000 diffractometer with Bragg–Brentano geometry. Diffraction patterns were obtained using CuK_α radiation (the wavelength 0.1540598 nm). The residual stresses $\sigma_1 + \sigma_2$ [17] were estimated from the shift of the α -Ti 103 diffraction peak. The rolled Ti-6Al-4V samples an-

nealed to relieve internal stresses were taken as a standard. The volume fraction of the α and β phases was determined by summing the intensities of the phase lines.

Vickers microhardness was measured in the upper part of the welds using a PMT-3 hardness tester with the indentation load 50 g. Metallographic and X-ray diffraction investigations as well as microhardness measurements were carried out in cross sections at the beginning and end of the weld (Fig. 1). The front and rear surfaces of the rectangular bars were previously ground to a depth of 1 mm.

3. RESULTS OF INVESTIGATION

3.1. Weld Microstructure of Rolled Ti-6Al-4V Samples

After chemically etching, the lateral surface of welds of the rolled Ti-6Al-4V samples reveals three distinct zones: weld metal (WM), the heat-affected zone (HAZ), and unaffected base metal (BM) (Fig. 2). The weld width is significantly different at its beginning and end. Thus, the initial weld width measured near the weld face is 4.5 mm and decreases to 2.8 mm towards its end. The width of the heat-affected zone has similar values at the beginning and end of the weld and amounts to 1.0 and 1.1 mm, respectively. In addition, the weld penetration depth continuously increases towards the end. The depth of

Table 2. Electron beam parameters

Current, mA	Accelerating voltage, kV	Welding speed, mm/s	Oscillation frequency, Hz	Hot spot diameter, mm	Sweep
60	40	15	1000	3	Spiral

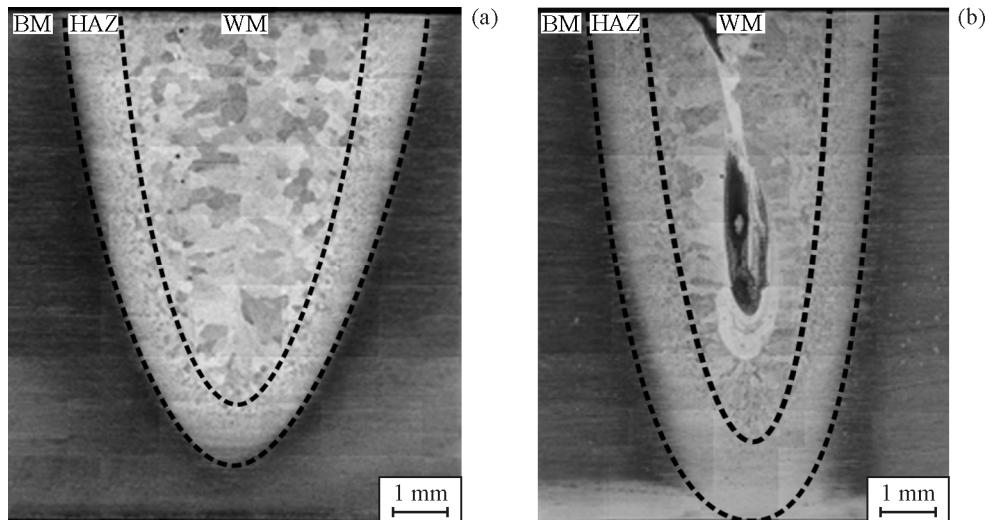


Fig. 2. Images taken at the beginning (a) and end (b) of the weld of the rolled Ti-6Al-4V samples. BM—base metal, HAZ—heat-affected zone, WM—weld metal.

penetration at the beginning of the weld does not exceed 0.9 of the thickness of the Ti-6Al-4V sample, while there is a keyhole at the end of the weld. The heat-affected zone visible at the weld root in Fig. 2b is explained by preliminary grinding of the outer layer.

The microstructure of the weld metal at the beginning of the weld consists of equiaxed and columnar primary β grains with the average transverse size 150 μm . Equiaxed grains are formed predominantly near the weld face (Fig. 3a), while columnar grains perpendicular to the weld axis are located closer to the weld root (Fig. 3b). The grains contain crystals of lath martensite $\sim 1 \mu\text{m}$ in thickness and $\sim 5\text{--}15 \mu\text{m}$ in length (Fig. 4a).

At the end of the weld of the rolled Ti-6Al-4V samples, there are also equiaxed and columnar primary β grains with the α' -Ti martensitic phase. Both primary β grains and martensitic α' plates have the

same size at the beginning and end of the weld. At the end of the weld, a narrow extended region, $\sim 500 \mu\text{m}$ wide, is formed around the weld axis (Fig. 2b). The microstructure of this region consists of misoriented quasi-equiaxed β -Ti grains with an average size of 10 μm (Fig. 5a). As can be seen from Table 3, along with titanium, aluminum, and vanadium, β -Ti grains are rich in iron and carbon. Electron microscopic images taken with the backscattered electron detector clearly demonstrate iron-rich dendritic crystals inside the β -Ti grains (Figs. 5b–5d). There are also numerous pores and cracks around the weld axis, propagating along grain boundaries (Figs. 5b, 5c). The pore size varies from 0.5 to 3 μm .

The microstructure of the heat-affected zone both at the beginning and at the end of the weld of the rolled Ti-6Al-4V samples is represented by equiaxed primary β grains. Their size reaches 30 μm near the weld metal and gradually decreases as the base metal

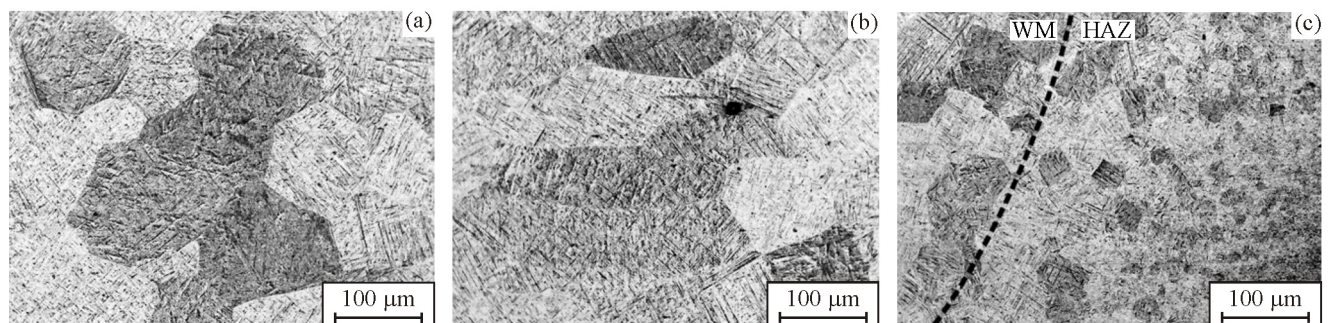


Fig. 3. Microstructure of the weld metal (a, b) and heat-affected zone (c) of the rolled Ti-6Al-4V samples. The images are taken at the beginning of the weld near its face (a, c) and root (b).

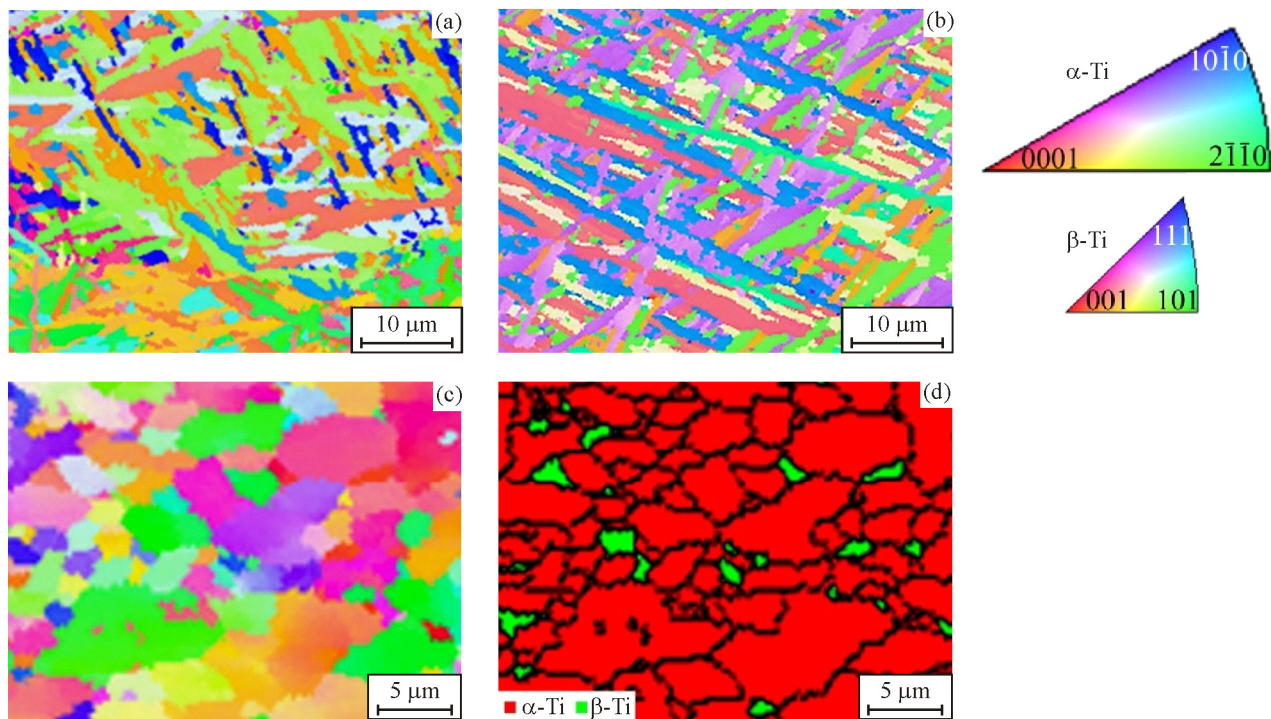


Fig. 4. EBSD orientation maps of the microstructure (a–c) and phase distribution (d) in the weld metal (a), heat-affected zone (b), and base metal (c, d) of the rolled Ti-6Al-4V samples. The images are taken at the beginning of the weld (color online).

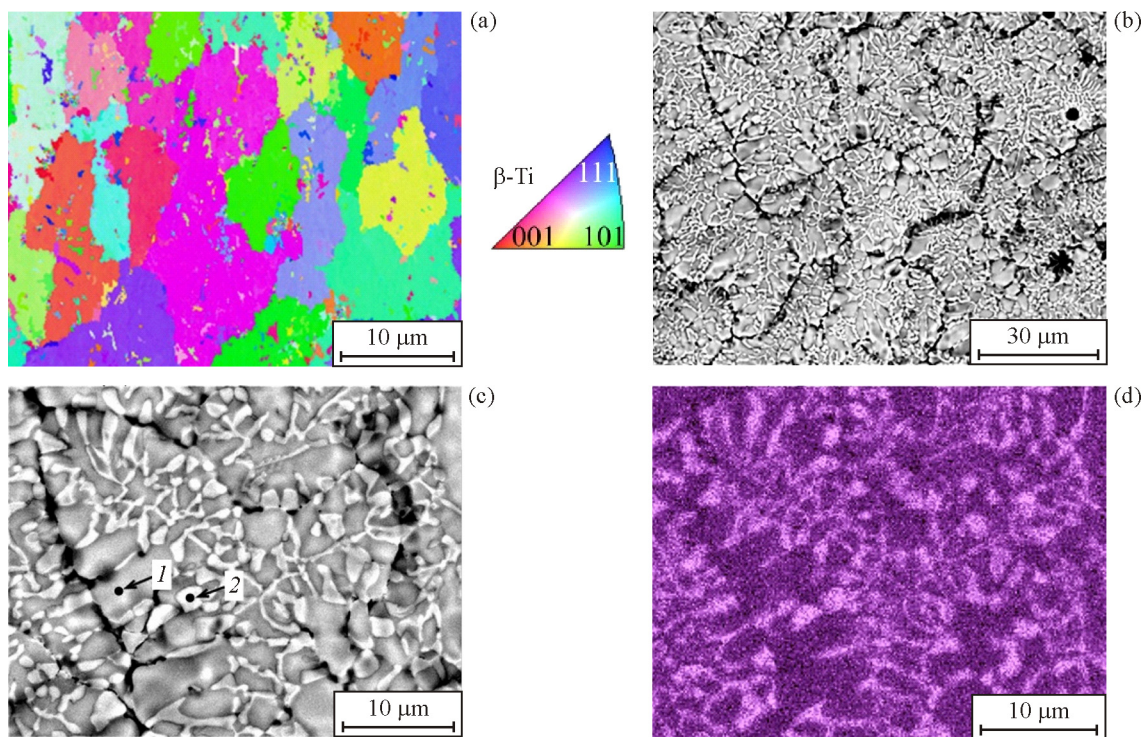


Fig. 5. EBSD orientation map (a) and electron microscopic images of the microstructure (b, c) as well as Fe distribution map (d) along the weld axis of the rolled Ti-6Al-4V samples. Images are taken at the end of the weld (color online).

Table 3. Elemental composition of the weld metal of Ti-6Al-4V samples

Elements	Point 1, Fig. 5c, wt %	Point 2, Fig. 5c, wt %	Point 3, Fig. 9b, wt %	Point 4, Fig. 9b, wt %
Ti	61.1	51.8	57.9	52.6
Al	4.4	2.8	5.3	1.7
V	3.8	2.4	3.9	2.6
Fe	23.6	38.2	21.8	40.6
C	7.1	4.8	11.1	2.5

is approached (Fig. 3c). Primary β grains in the heat-affected zone contain predominantly lamellar martensite consisting of thin plates (needles) of the α' phase (Fig. 4b). The martensitic α' plates in the heat-affected zone are much larger than those in the weld metal.

The microstructure of the base metal of the rolled Ti-6Al-4V samples consists of differently orientated equiaxed α -Ti grains, the average size of which is $5\ \mu\text{m}$ (Fig. 4c). Figure 4d shows that the globular β phase with the volume fraction 5% precipitates at the triple junctions of the α grains. This is in good agreement with the results of the previous electron microscopic studies [18].

3.2. Weld Microstructure of 3D Printed Ti-6Al-4V Samples

As with the rolled Ti-6Al-4V samples, the geometric dimensions of the weld of the 3D printed Ti-6Al-4V samples change continuously along the weld. As can be seen from Fig. 6, the weld width reaches 5.8 mm at the beginning of the weld and decreases to

5.1 mm at its end. The depth of penetration of the 3D printed samples, on the contrary, increases along the weld, being comparable with that of the rolled Ti-6Al-4V samples. However, the width of the heat-affected zone hardly changes along the weld of the 3D printed samples and amounts to $\sim 0.6\ \text{mm}$.

In the weld metal of the 3D printed Ti-6Al-4V samples, coarse equiaxed primary β grains and columnar primary β grains perpendicular to the weld axis are also formed (Figs. 6 and 7a). The average transverse size of the primary β grains at the beginning and end of the weld is 2 mm. Primary β grains have a lamellar morphology due to the formation of a martensitic structure (Fig. 8a). Comparison of Figs. 4a and 8a shows that the martensitic laths of the α' phase in the weld metal of the 3D printed samples are larger than those in the weld metal of the rolled samples.

In the 3D printed Ti-6Al-4V samples, a narrow ($600\text{-}\mu\text{m}$ -wide) region is also formed around the weld axis, which consists of equiaxed grains $30\text{--}50\ \mu\text{m}$ in size (Fig. 7b) with significantly different crystal structure at the beginning and at the end of the

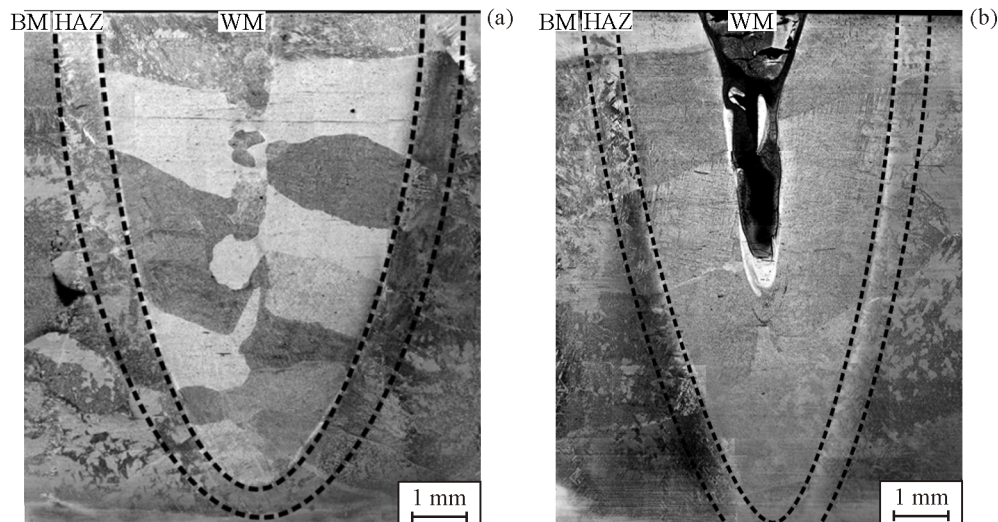


Fig. 6. Images taken at the beginning (a) and end (b) of the weld of the 3D printed Ti-6Al-4V samples.

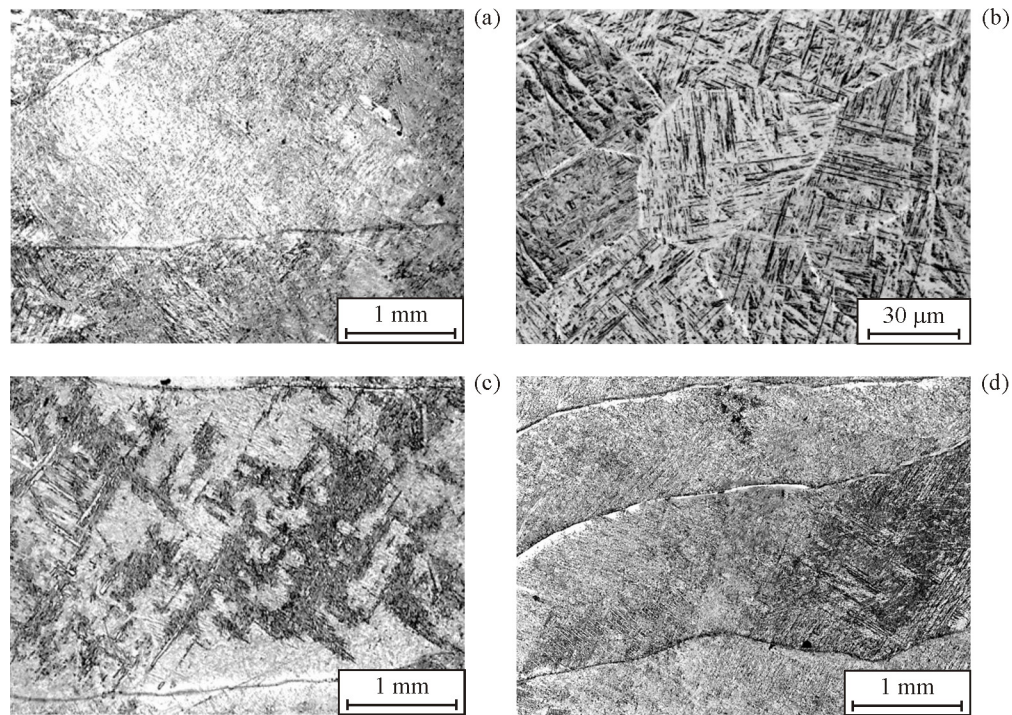


Fig. 7. Microstructure of the weld metal (a, b), heat-affected zone (c), and base metal (d) of the 3D printed Ti-6Al-4V samples. Images are taken at the beginning of the weld.

weld. The grains at the beginning of the weld consist of α' -phase plates, while the grains at the end of the weld contain the β phase and dendritic crystals with the iron concentration 40% (Fig. 9, Table 3). Similar to the welds of the rolled Ti-6Al-4V specimens, pores and cracks are observed at the end of the weld of the 3D printed Ti-6Al-4V samples. The average pore size is 2 μm .

The microstructure of the heat-affected zone at the beginning and end of the weld of the 3D printed Ti-6Al-4V samples consists of columnar primary β grains with α' -phase plates. The transverse size of columnar grains in the heat-affected zone is ~ 3 mm (Fig. 7c), which coincides with the grain size in the base metal (Fig. 7d). The transverse size of the mar-

tensite plates inside the primary β grains in the heat-affected zone (Fig. 8b) is larger than that in the weld metal (Fig. 8a) and base metal (Fig. 8c).

3.3. X-Ray Diffraction Analysis

The analysis of the diffraction patterns of the rolled Ti-6Al-4V samples shows that welding has an insignificant effect on the α -Ti peak intensity but leads to a decrease in the 110 peak intensity of the β phase (Fig. 10a). As can be seen from Table 4, the volume fraction of the β phase is 7.5% in the base metal and decreases to 3.7 and 2.3% at the beginning and end of the weld, respectively.

Crystallites of the α phase formed in the 3D printed Ti-6Al-4V samples during electron beam welding

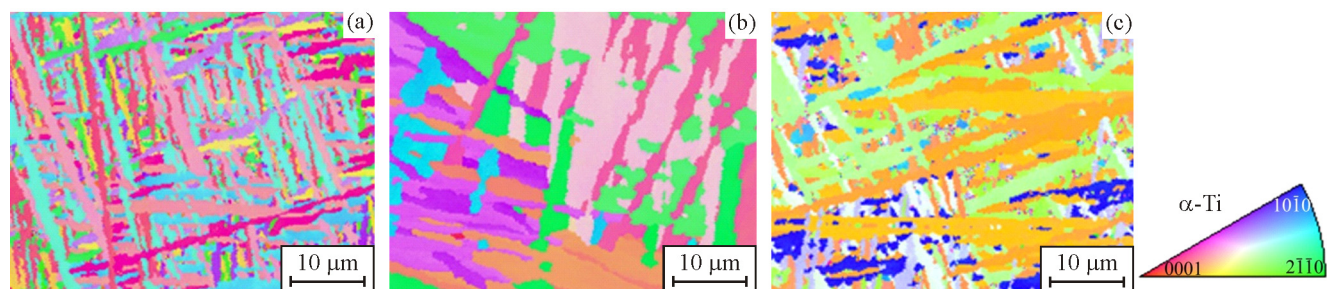


Fig. 8. EBSD orientation maps of the microstructure of the weld metal (a), heat-affected zone (b), and base metal (c) of the 3D printed Ti-6Al-4V samples. Images are taken at the beginning of the weld (color online).

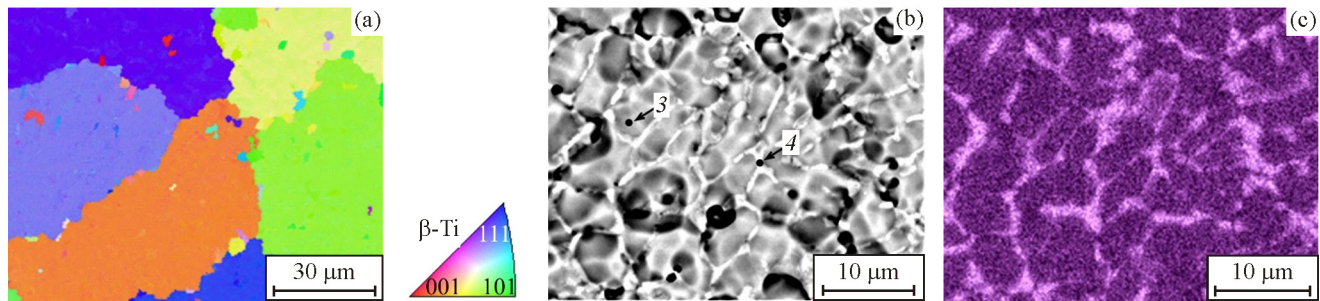


Fig. 9. EBSD orientation map (a) and electron microscopic image of the microstructure (b) as well as Fe distribution map (c) in the vapor capillary at the end of the weld of the 3D printed Ti-6Al-4V samples (color online).

have predominantly the [100] orientation (Fig. 10b). In addition, there is a diffraction peak at $2\theta = 42.4^\circ$ at the end of the weld, which corresponds to the TiFe intermetallic compound with the volume fraction 2.4% (Fig. 10b, curve 3, Table 4). In this case, on both sides of the weld of the 3D printed Ti-6Al-4V samples, the volume fraction of the residual β phase is significantly reduced compared to the base metal.

As can be seen from Table 4, the base metal of the rolled and 3D printed Ti-6Al-4V samples is under compressive stresses. At the beginning of the welds of both samples, the stresses are still compressive, but they become tensile at the end of the welds.

3.4. Hardness Measurements

The microhardness of the rolled Ti-6Al-4V samples does not exceed 4100 MPa. As can be seen from Fig. 11a, at the beginning of the weld, the microhardness in the weld metal and heat-affected zone is 5200 and 4800 MPa, respectively. At the end of the weld, the microhardness in the weld metal is no more than 4500 MPa but reaches 11 600 MPa in the narrow re-

gion around the weld axis. The microhardness of the heat-affected zone is 4100 MPa.

In the weld of the 3D printed Ti-6Al-4V samples, the microhardness is similarly distributed. The diagram of cross-sectional microhardness distribution also reveals regions corresponding to weld metal, including its central part enriched in iron and other alloying elements, the heat-affected zone, and base metal (Fig. 11b). The size of these zones agrees well with the results of metallographic studies. In this case, the microhardness in the weld of the 3D printed samples is comparable with that in the weld of the rolled Ti-6Al-4V samples.

4. DISCUSSION OF RESULTS

Electron beam melting of the surface of a welded sample is accompanied by the formation of a temperature gradient and consequently a surface tension gradient in the melt pool surface [19]. As a result, the melt flows (thermocapillary effect) in the direction opposite to the temperature gradient, i.e. from the edge of the melt pool to the center. Near the bottom

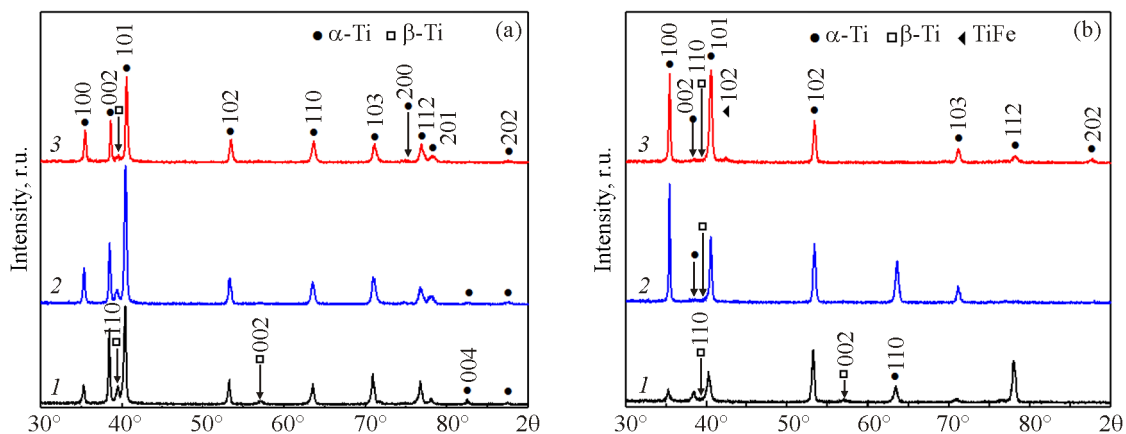


Fig. 10. X-ray diffraction patterns of the Ti-6Al-4V samples produced by rolling (a) and 3D printing (b): 1—base metal; 2—beginning of the weld; 3—end of the weld (color online).

Table 4. Volume fraction of the phases and internal stresses in the studied Ti-6Al-4V samples

Initial state		Volume fraction, wt %			$\sigma_1 + \sigma_2$, MPa
		α -Ti	β -Ti	TiFe	
Rolling	Base metal	92.5	7.5	–	–650
	At the beginning of the weld	96.3	3.7	–	–380
	At the end of the weld	97.7	2.3	–	140
3D printing	Base metal	96.1	3.9	–	–790
	At the beginning of the weld	99.2	0.8	–	–110
	At the end of the weld	96.9	0.7	2.4	100

of the melt pool, there appears a flow from the melt pool center to the edge. At a relatively low power density of the electron beam (up to 10^5 W/cm²), the melt pool takes on a spherical shape, which makes this mode of electron beam welding (incomplete-penetration welding) applicable to thin-walled products.

The studied 10-mm-thick Ti-6Al-4V samples are welded in the deep-penetration mode with the formation of a vapor capillary. In this mode, use is made of the electron beam of the critical power density (10^9 – 10^{10} W/cm² [20]), at which the metal is heated much faster than the rate of heat transfer to the base metal due to thermal conductivity. Under these conditions, a local zone with the temperature exceeding the boiling point of the melt is formed on the surface of the welded part. The recoil force of the expanding vapor acting on the surrounding molten metal causes an intense downward flow, which can effectively transfer the molten metal to the pool bottom, forming complete-penetration welds. After reaching the bottom of

the melt pool, the flow is forced to the melt pool tail, from where the swirling flow moves upward (Fig. 1b).

Welds of the rolled and 3D printed Ti-6Al-4V samples have different geometric dimensions since the thermal conductivity of metals significantly depends on their microstructure. Grain boundaries can be generally considered as obstacles to heat transfer, so the thermal conductivity of polycrystalline materials, as a rule, decreases with grain refinement [21]. The 3D printed Ti-6Al-4V samples have larger primary β grains than the rolled samples, and therefore they are characterized by higher thermal conductivity. Thus, the 3D printed Ti-6Al-4V samples have wider welds, as determined by the rate of heat transfer in the direction perpendicular to the electron beam. On the other hand, the higher thermal conductivity of the 3D printed Ti-6Al-4V samples allows for a faster cooling rate of the welds. According to [22], a high cooling rate of the molten metal limits the

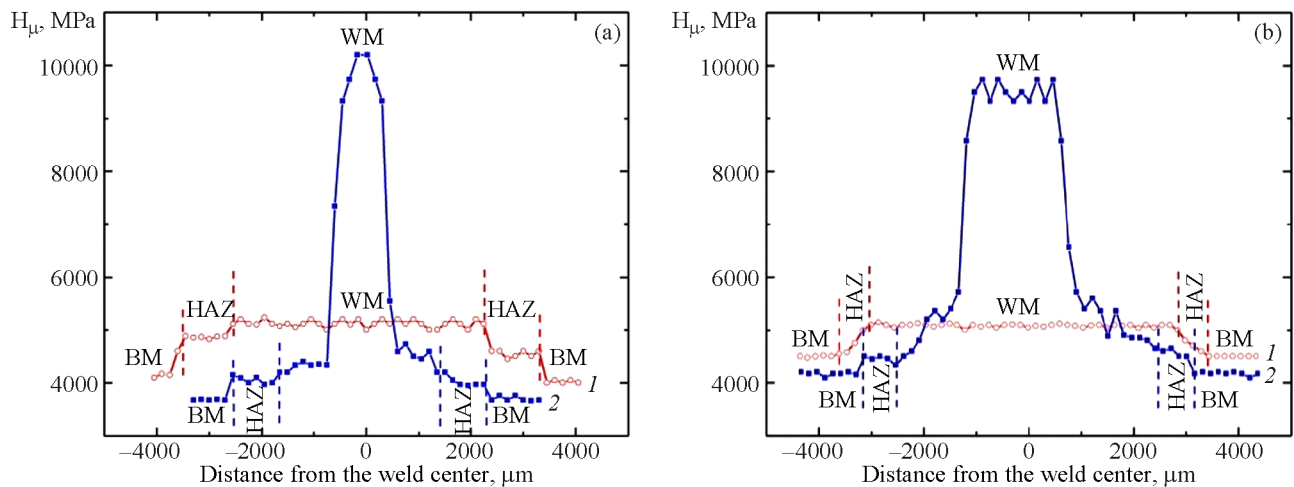


Fig. 11. Cross-sectional microhardness distribution in the welds of the Ti-6Al-4V samples produced by rolling (a) and 3D printing (b): 1—beginning of the weld, 2—end of the weld (color online).

growth of crystallites in the weld metal and reduces the size of the heat-affected zone. In our experiments, the heat-affected zone in the 3D printed Ti-6Al-4V samples proves to be half as wide as that in the rolled samples. The higher cooling rate of the melt pool in the 3D printed Ti-6Al-4V samples is also confirmed by the lower volume fraction of the residual β phase in the weld metal as compared to the rolled samples.

A gradual increase in the thermal conductivity of the welded Ti-6Al-4V samples due to heating [23] causes a deeper penetration at the end of the weld as compared to the beginning. Thus, the weld penetration coefficient (depth-to-width ratio) for the rolled Ti-6Al-4V samples is $K=1.7$ and increases to $K=2.0$ at the end of the weld. The penetration coefficient for the 3D printed Ti-6Al-4V samples is $K=1.5$ at the beginning of the weld and 1.7 at the end.

The microstructural changes observed in the Ti-6Al-4V samples during electron beam welding are associated with the influence of the vapor capillary on the melt pool formation. As the electron beam moves, the metal melts on the front wall of the vapor capillary and crystallizes on the rear wall. Primary β grains are formed on the base metal grains surrounding the melt pool, growing in the direction opposite to the heat removal direction, i.e. towards each other along the weld axis. The columnar grains inherit the size of the base metal grains, which points to their epitaxial growth.

On the weld face, the melt cools much slower than near the weld root, which is due to upward flows of the molten metal that long retain heat. In addition, the heat removal rate near the sample surface is significantly lower than within the sample. Therefore, primary β grains at the weld face of the rolled Ti-6Al-4V samples take on an equiaxed shape during melt crystallization (Fig. 2a). The transverse size of columnar primary β grains at the weld face of the 3D printed Ti-6Al-4V samples turns out to be larger than at the weld root (Fig. 6a).

With further cooling, an acicular α' phase is formed inside the primary β grains located in the weld metal and in the heat-affected zone of the studied Ti-6Al-4V samples. According to [24], the high-temperature β phase undergoes a diffusion-free (martensitic) $\beta \rightarrow \alpha'$ transformation at the cooling rate of titanium alloy Ti-6Al-4V above 410°C/s . The acicular/lamellar α' phase is, in fact, a supersaturated α -Ti-based solid solution with the crystal lattice distorted by vanadium atoms. The low volume fraction of the residual β phase in the weld metal is an indirect confirmation of the presence of vanadium in the α'

phase. Note that the acicular α' phase is usually formed during electron beam or laser welding of Ti-6Al-4V samples, while the microstructure of argon arc welds is presented by a mixture of the α and α' phases [25]. The latter is due to the fact that argon arc welding is characterized by a larger heating area and higher power density compared to electron beam welding [26] and consequently a slower cooling rate of the melt pool.

A high temperature gradient present in electron beam welds leads to the formation of different martensitic structures in the weld metal and heat-affected zone of the studied samples. High-temperature lath martensite is formed in the weld metal that has the maximum temperature, and low-temperature lamellar martensite is found in the heat-affected zone.

In the 3D printed Ti-6Al-4V samples, fine equiaxed primary β grains are seen near the weld axis. The reasons for the formation of fine globular grains are a small temperature gradient in the center of the melt pool associated with the release of latent heat of weld solidification and with concentration undercooling caused by the segregation of alloying elements in front of the crystallization front. The effect of concentration undercooling is most pronounced at the end of the weld where a thin layer enriched in iron and carbon is formed in front of the crystallization front. The increased content of iron, which is a β stabilizer, determines the nucleation and growth of globular primary β grains in the center of the melt pool, in which the intermetallic TiFe phase precipitates. In addition, iron preserves the bcc lattice in the β grains during subsequent cooling of the welds to room temperature.

In this work, the parameters of electron beam welding are chosen to form a deep-penetration weld without visible defects. However, the welding parameters are not optimum since they were chosen without taking into account the increase in the penetration depth during heating. At the end of the weld, the vapor capillary not only passes through the thickness of the studied Ti-6Al-4V samples, but also penetrates into the underlying plate made of stainless steel 12Cr18Ni10Ti. This defect can be eliminated by increasing the welding speed, which will reduce the penetration depth at the end of the weld, or by gradually shifting the focal plane of the electron beam towards the upper surface of the Ti-6Al-4V samples during the welding process. Nevertheless, the results obtained are illustrative of the behavior of the molten metal inside the vapor capillary.

During electron beam welding, the liquid metal moves from top to bottom along the front wall of the vapor capillary. After reaching the bottom, the metal is forced to the rear wall, where it swirls and rises to the upper part of the capillary. At the end of the weld, where the Ti-6Al-4V samples are completely penetrated, an electron beam arrives at the steel substrate, causing its heating and melting. As a result, the metal around the weld axis becomes enriched in chemical elements of the 12Cr18Ni10Ti substrate. The high content of Fe, which is the eutectoid β stabilizer, leads to the formation of dendritic equiaxed β -Ti grains along the weld axis of the Ti-6Al-4V samples, in which the TiFe intermetallic phase precipitates. The low volume fraction of the TiFe phase (~ 2 vol%) determined by X-ray diffraction may be due to the fact that this phase is nanocrystalline. Intermetallic compounds formed in the titanium-iron system are known to significantly increase the strength of the weld but strongly reduce its ductility [27]. The precipitation of the intermetallic phase inside the vapor capillary causes centerline cracking in the welds under tensile stresses induced by fully or partially coherent boundaries between phases with different lattices.

Though the rolled Ti-6Al-4V samples are completely penetrated, the heat-affected zone seen at the end of the weld indicates that the electron beam does not reach the substrate material (Fig. 2b). This situation can be explained by the fact that the outer 1-mm-thick layer was ground from the metallographic samples. It is this outermost ground layer (at the very end of the weld) where the beam arrives at the steel substrate. However, since the melt pool has an elongated shape (Fig. 1b), only its tail part, which is rich in iron, is observed at a distance of 1 mm from the end of the weld.

The main reason for the development of tensile residual stresses in welds is shrinkage of the metal during the liquid-solid transition. In this case, the value and sign of residual stresses are governed by different cooling rates of the metal at the weld face and root, as well as by martensitic transformations in the weld metal and heat-affected zone [28]. According to [29], martensitic $\beta \rightarrow \alpha'$ transformations in the weld of the Ti-6Al-4V samples can not only relieve tensile stresses but also induce compressive residual stresses. In our experiments, equiaxed primary β grains containing the martensitic α' phase are formed at the beginning of the weld of the studied Ti-6Al-4V samples, and β -Ti grains with the intermetallic TiFe phase are found at the end of the weld. As a result,

the residual stresses are compressive at the beginning of the weld and tensile at the end.

5. CONCLUSIONS

The paper studied the microstructure and phase composition of electron beam welded Ti-6Al-4V titanium alloy produced by rolling and wire-feed electron beam additive manufacturing. It was shown that deep-penetration electron beam welding was accompanied by the formation of columnar primary β grains near the weld root and equiaxed primary β grains near the weld face and around the weld axis. Fast cooling caused the martensitic α' phase to crystallize in the primary β grains in the form of thin laths grouped into packets. In the heat-affected zone, the formed primary β grains contained lamellar martensite. Both the weld metal and the heat-affected zone were characterized by a low volume fraction of the residual β phase.

Welded joints of the 3D printed Ti-6Al-4V samples were found to be wider than those of the rolled Ti-6Al-4V samples. This widening was associated solely with an increase in the weld width. The heat-affected zone in the 3D printed Ti-6Al-4V samples was two times narrower than in the rolled samples. In addition, welds of the 3D printed Ti-6Al-4V samples had a lower volume fraction of the residual β phase compared to the rolled samples.

During electron beam welding of Ti-6Al-4V samples, the penetration depth continuously increased along the weld. Nonoptimum welding parameters (primarily positioning of the focal plane of the electron beam relative to the welded surface) lead to melting of the 12Cr18Ni10Ti substrate at the end of the weld. As a result, a narrow (~ 500 μm) extended region with equiaxed grains 30–50 μm in size was formed along the weld axis. The grains contained a β phase and dendritic TiFe crystals.

Deep-penetration electron beam welding caused the same increase in the microhardness of the rolled and 3D printed Ti-6Al-4V samples. It was shown that the microhardness both in the weld metal and heat-affected zone of the studied samples was 5200 and 4800 MPa, respectively. The microhardness in the weld region containing the intermetallic TiFe phase reached 11 600 MPa.

ACKNOWLEDGMENTS

The research was carried out using the equipment of the Nanotech Shared Use Center of ISPMS SB

RAS and the Shared Use Center of the Innovation Center for Nanomaterials and Nanotechnologies of TPU.

FUNDING

The work was performed within the government statement of work for ISPMS SB RAS (research line FWRW-2021-0010).

OPEN ACCESS

This article is licensed under a Creative Commons Attribution 4.0 International License, which permits use, sharing, adaptation, distribution and reproduction in any medium or format, as long as you give appropriate credit to the original author(s) and the source, provide a link to the Creative Commons license, and indicate if changes were made. The images or other third party material in this article are included in the article's Creative Commons license, unless indicated otherwise in a credit line to the material. If material is not included in the article's Creative Commons license and your intended use is not permitted by statutory regulation or exceeds the permitted use, you will need to obtain permission directly from the copyright holder. To view a copy of this license, visit <http://creativecommons.org/licenses/by/4.0/>

CONFLICT OF INTEREST

The authors of this work declare that they have no conflicts of interest.

REFERENCES

- Herzog, D., Seyda, V., Wycisk, E., and Emmelmann, C., Additive Manufacturing of Metals, *Acta Mater.*, 2016, vol. 117, pp. 371–392. <https://doi.org/10.1016/j.actamat.2016.07.019>
- Sames, W.J., List, F.A., Pannala, S., Dehoff, R.R., and Babu, S.S., The Metallurgy and Processing Science of Metal Additive Manufacturing, *Int. Mater. Rev.*, 2016, vol. 61, pp. 315–360. <https://doi.org/10.1080/09506668.2015.1116649>
- Rautio, T., Hamada, A., Mäkikangas, J., Jaskari, M., and Järvenpää, A., Laser Welding of Selective Laser Melted Ti6Al4V: Microstructure and Mechanical Properties, *Mater. Today. Proc.*, 2020, vol. 28, no. 2, pp. 907–911. <https://doi.org/10.1016/j.matpr.2019.12.322>
- Yu, H., Li, F., Yang, J., Shao, J., Wang, Z., and Zen, X., Investigation on Laser Welding of Selective Laser Melted Ti-6Al-4V Parts: Weldability, Microstructure and Mechanical Properties, *Mater. Sci. Eng. A*, 2018, vol. 712, pp. 20–27. <https://doi.org/10.1016/j.msea.2017.11.086>
- Vock, S., Klöden, B., Kirchner, A., Weißgärber, T., and Kieback, B., Powders for Powder Bed Fusion: A Review, *Prog. Addit. Manuf.*, 2019, vol. 4, pp. 383–397. <https://doi.org/10.1007/s40964-019-00078-6>
- Ahn, D.G., Directed Energy Deposition (DED) Process: State of the Art, *Int. J. Precis. Eng. Manuf. Green Technol.*, 2021, vol. 8, p. 703. <https://doi.org/10.1007/s40684-020-00302-7>
- Razorenov, S.V., Garkushin, G.V., Savinykh, A.S., Klimova-Korsmik, O.G., Shalnova, S.A., and Gushchina, M.O., Dynamic Strength of VT6 Titanium Alloy Manufactured by Laser Metal Deposition, *Phys. Mesomech.*, 2022, vol. 25, no. 1, pp. 26–32. <https://doi.org/10.1134/S1029959922010040>
- Xu, M., Chen, Y., Zhang, T., Deng, H., and Ji, D., Effects of Solution Treatment on Laser Welding of Ti-6Al-4V Alloy Plate Produced through Wire Arc Additive Manufacturing, *Metals*, 2020, vol. 10, p. 1310. <https://doi.org/10.3390/met10101310>
- Omoniyi, P.O., Mahamood, R.M., Arthur, N., Pityana, S., Skhosane, S., Okamoto, Y., Shinonaga, T., Maina, M.R., Jen, T.C., and Akinlabi, E.T., Joint Integrity Evaluation of Laser Beam Welded Additive Manufactured Ti6Al4V Sheets, *Sci. Rep.*, 2022, vol. 12, p. 4062. <https://doi.org/10.1038/s41598-022-08122-2>
- Wits, W.W. and Jauregui Becker, J.V., Laser Beam Welding of Titanium Additive Manufactured Parts, *Proc. CIRP 28*, 2015, pp. 70–75. <https://doi.org/10.1016/j.procir.2015.04.013>
- Katayama, S., *Handbook of Laser Welding Technologies*, Cambridge: Woodhead Pub., 2013.
- Kalashnikov, K., Chumaevskii, A., Kalashnikova, T., Cheremnov, A., Moskvichev, E., Amirov, A., Krasno-veikin, V., and Kolubaev, E., Friction Stir Processing of Additively Manufactured Ti-6Al-4V Alloy: Structure Modification and Mechanical Properties, *Metals*, 2022, vol. 12, p. 55. <https://doi.org/10.3390/met12010055>
- Weglowski, M.S., Blacha, S., and Phillips, A., Electron Beam Welding—Techniques and Trends—Review, *Vacuum*, 2016, vol. 130, pp. 72–92. <https://doi.org/10.1016/j.vacuum.2016.05.004>
- Wang, S. and Wu, X., Investigation on the Microstructure and Mechanical Properties of Ti-6Al-4V Alloy Joints with Electron Beam Welding, *Mater. Design*, 2012, vol. 36, pp. 663–670. <https://doi.org/10.1016/j.matdes.2011.11.068>
- Chen, X., Zhang, J., Chen, X., Cheng, X., and Huang, Z., Electron Beam Welding of Laser Additive Manufacturing Ti-6.5Al-3.5Mo-1.5Zr-0.3Si Titanium Alloy Thick Plate, *Vacuum*, 2018, vol. 151, pp. 116–121. <https://doi.org/10.1016/j.vacuum.2018.02.011>
- Boyangin, E.N., Perevalova, O.B., Panin, A.V., and Martynov, S.A., The Effect of Electron Beam Welding on the Microstructure and Microhardness of 3D-Print

- ed Products from Titanium Alloy Ti-6Al-4V, *PMM*, 2021, vol. 122, no. 2, pp. 141–147.
17. Mirkin, L.I., *Handbook of X-ray Structure Analysis of Polycrystalline Materials*, New York: Plenum Press, 1964.
 18. Sinyakova, E.A., Panin, A.V., Perevalova, O.B., Shugurov, A.R., Kalashnikov, M.P., and Teresov, A.D., The Effect of Phase Transformations on the Elastic Recovery of Pulsed Electron Beam Irradiated Ti-6Al-4V Titanium Alloy during Scratching, *J. Alloys Compd.*, 2019, vol. 795, pp. 275–283. <https://doi.org/10.1016/j.jallcom.2019.04.320>
 19. Paton, B.E., Yushchenko, K.A., Kovalenko, D.V., Krivtsun, I.V., Demchenko, V.F., and Kovalenko, I.V., Role of Keyhole in Formation of Deep Penetration in A-TIG Welding of Stainless Steel, *The Paton Welding J.*, 2006, no. 6, pp. 2–6.
 20. Olshanskaya, T.V., Fedoseeva, E.M., and Koleva, E.G., Creation of Thermal Models at Electron Beam Welding by Method of Function of Green, *Vestn. PNIPU. Mashinostr. Materialoved.*, 2017, vol. 19, no. 3, pp. 49–74.
 21. Dong, H., Wen, B., and Melnik, R., Relative Importance of Grain Boundaries and Size Effects in Thermal Conductivity of Nanocrystalline Materials, *Sci. Rep.*, 2014, vol. 4, p. 7037. <https://doi.org/10.1038/srep07037>
 22. Kolubaev, A.V., Sizova, O.V., Kolubaev, E.A., Zaikina, A.A., Vorontsov, A.V., Denisova, Yu.A., and Rubtsov, V.E., Structural Features of Laser Welded 13Mn6 Constructional Steel, *Obrab. Met.*, 2018, vol. 20, no. 3, pp. 123–133. <https://doi.org/10.17212/1994-6309-2018-20.3-123-133>
 23. Koniarczyk, P., Zmywaczyk, J., Ślęzak, T., and Zieliński, M., Thermal Diffusivity and Thermal Expansion Investigations of Titanium Grade 5, *AIP Conf. Proc.*, 2021, vol. 2429, p. 020045-1-7. <https://doi.org/10.1063/5.0069644>
 24. Ahmed, T. and Rack, H.J., Phase Transformations during Cooling in $\alpha + \beta$ Titanium Alloys, *Mater. Sci. Eng. A*, 1998, vol. 243, pp. 206–211. [https://doi.org/10.1016/s0921-5093\(97\)00802-2](https://doi.org/10.1016/s0921-5093(97)00802-2)
 25. Rae, W., Lomas, Z., Jackson, M., and Rahimi, S., Measurements of Residual Stress and Microstructural Evolution in Electron Beam Welded Ti-6Al-4V Using Multiple Techniques, *Mater. Charact.*, 2017, vol. 132, pp. 10–19. <https://doi.org/10.1016/j.matchar.2017.07.042>
 26. Baranov, D.A., Zhatkin, S.S., Nikitin, K.V., Parkin, A.A., Shchedrin, E.Yu., and Deev, V.B., Study of the Influence of Different Energy Sources on the Structure and Mechanical Properties of a Welded Joint from an EP693 Nickel Alloy, *Russ. J. Non-Ferr. Met.*, 2022, vol. 63, pp. 57–62.
 27. Li, W., Yan, L., Karnati, S., Liou, F., Newkirk, J., Taminger, K.M.B., and Seufzer, W.J., Ti-Fe Intermetallics Analysis and Control in Joining Titanium Alloy and Stainless Steel by Laser Metal Deposition, *J. Mater. Process. Technol.*, 2017, vol. 242, pp. 39–48. <https://doi.org/10.1016/j.jmatprotec.2016.11.010>
 28. Shiga, C., Mraz, L., Bernasovsky, P., Hiraoka, K., Mikula, P., and Vrana, M., Residual Stress Distribution of Steel Welded Joints with Weld Metal of Low Martensite Transformation Temperature, *Weld. World*, 2007, vol. 51, nos. 11–12, pp. 11–19. <https://doi.org/10.1007/BF03266604>
 29. Mehdi, B., Badji, R., Ji, V., Allil, B., Bradai, D., Deschaux-Beaume, F., and Soulié, F., Microstructure and Residual Stresses in Ti-6Al-4V Alloy Pulsed and Unpulsed TIG Welds, *J. Mater. Process. Technol.*, 2016, vol. 231, pp. 441–448. <https://doi.org/10.1016/j.jmatprotec.2016.01.018>